



**HAL**  
open science

## Deriving the angular response function for backscattering sensors

Xiaodong Zhang, Edouard Leymarie, Emmanuel Boss, Lianbo Hu

► **To cite this version:**

Xiaodong Zhang, Edouard Leymarie, Emmanuel Boss, Lianbo Hu. Deriving the angular response function for backscattering sensors. *Applied optics*, 2021, 60 (28), pp.8676-8687. 10.1364/AO.437735 . hal-03352678

**HAL Id: hal-03352678**

**<https://hal.science/hal-03352678>**

Submitted on 12 Jan 2022

**HAL** is a multi-disciplinary open access archive for the deposit and dissemination of scientific research documents, whether they are published or not. The documents may come from teaching and research institutions in France or abroad, or from public or private research centers.

L'archive ouverte pluridisciplinaire **HAL**, est destinée au dépôt et à la diffusion de documents scientifiques de niveau recherche, publiés ou non, émanant des établissements d'enseignement et de recherche français ou étrangers, des laboratoires publics ou privés.



# Deriving the angular response function for backscattering sensors

XIAODONG ZHANG,<sup>1,\*</sup> EDOUARD LEYMARIE,<sup>2</sup> EMMANUEL BOSS,<sup>3</sup> AND LIANBO HU<sup>4</sup>

<sup>1</sup>Division of Marine Science, School of Ocean Science and Engineering, The University of Southern Mississippi, Stennis Space Center, Mississippi 39529, USA

<sup>2</sup>Laboratoire d'Océanographie de Villefranche, CNRS, Sorbonne Université, Villefranche-sur-Mer, France

<sup>3</sup>School of Marine Sciences, University of Maine, 5706 Aubert Hall, Orono, Maine 04473, USA

<sup>4</sup>Ocean Remote Sensing Institute, Ocean University of China, Qingdao 266003, China

\*Corresponding author: Xiaodong.zhang@usm.edu

Received 23 July 2021; revised 25 August 2021; accepted 30 August 2021; posted 30 August 2021 (Doc. ID 437735); published 23 September 2021

We derived the angular response function ( $W_N$ ) for scattering sensors that automatically satisfies the normalization criterion and its corresponding weight ( $W_T$ ).  $W_N$ 's, derived for two commercial sensors, HydroScat-6 (HOBI Labs) and ECO-BB (Sea-Bird Inc.), agrees well with the Monte Carlo simulation and direct measurements. The backscattering measured for microbeads of known sizes agrees better with Mie calculation when the derived  $W_N$  was applied. We deduced that the reduction of  $W_T$  with increasing attenuation coefficient is related to path length attenuation and showed that this theoretically derived correction factor performs better than the default methods for the two commercial backscattering sensors. The analysis conducted in this study also leads to an estimate of uncertainty budget for the two sensors. The major uncertainty for ECO-BB is associated with its angular response function because of its wide field of view, whereas the main uncertainty for the HydrScat-6 is due to attenuation correction because of its relatively long path length. © 2021 Optical Society of America

<https://doi.org/10.1364/AO.437735>

## 1. INTRODUCTION

Knowledge of light scattering provides important information on the propagation and dispersion of light and characteristics of particulate matter suspended in a water mass. Light scattering is quantified by the volume scattering function (VSF;  $m^{-1} sr^{-1}$ ) [1], which describes the angular dependence of scattered light for an incident unpolarized beam. The VSF at a given wavelength of light ( $\lambda$ ) is defined as a ratio of the intensity of light,  $dI(\theta, \lambda)$  ( $W sr^{-1}$ ) scattered by an infinitesimal water mass at a scattering angle  $\theta$ , to the product of incident irradiance  $dE(\lambda)$  ( $W m^{-2}$ ) and the volume  $dV$  ( $m^3$ ) of the water mass, i.e.,

$$\beta(\theta, \lambda) = \frac{dI(\theta, \lambda)}{dE(\lambda)dV}. \quad (1)$$

This definition has two implications. First, the VSF represents a single-scattering optical property; in other words, only those photons from the source that are scattered once by the sampling volume are considered. Second, the scattering angle should be well defined between the paths from the source to the scattering volume and from the scattering volume to the detector. Both requirements for measuring the VSF are often violated however, either due to operation conditions, instrument design, or both. For example, in turbid coastal waters where multiple scattering prevails, Doxaran *et al.* [2] simulated the effect of

multiple scattering and derived a correction that should be applied to improve the derivation of the VSF from the measured scattered light. If the field of view (FOV) of an instrument spans a relatively wide range of scattering angles, the received signal represents a cumulative contribution from the scattering at each of these angles. The function that describes how the VSFs at different scattering angles contributes to the VSF that the instrument measures is called the instrumental angular response function.

We denote this angular response function as  $W_N(\theta)$  (units of  $rad^{-1}$  or  $deg^{-1}$ ), where the subscript "N" stresses the fact that  $W_N$  should satisfy the normalization condition,

$$\int_0^\pi W_N(\theta) d\theta = 1. \quad (2)$$

With  $W_N$ , we define

$$\beta(\theta_0) = \int_0^\pi \beta(\theta) W_N(\theta) d\theta, \quad (3)$$

where  $\beta(\theta_0)$  represents  $W_N(\theta)$ -weighted mean value of  $\beta(\theta)$  and  $\theta_0$  is often called nominal scattering angle, whose exact value depends on both  $W_N(\theta)$  and  $\beta(\theta)$ . Note that for compactness, we have dropped the wavelength dependence of the VSF, as the angular weighting is derived from the sensor geometry.

Knowledge of  $W_N$  for a backscattering sensor is critical to properly interpret the measured signal and when calibrating the sensor [3]. For calibration, Maffione and Dana [4] measured the reflected signal of a Lambertian target at various distances from the sensor. Because the reflectance of the Lambertian target is known and the scattering angle for the type of backscattering sensor they studied increases with the distance, they showed that the variation of measured values with distance is related to  $W_N$ . However, as we will show later, because the scattering angle also changes with the horizontal displacement at a particular depth, the response function versus distance is not the same as  $W_N$ . To the best of our knowledge,  $W_N$  for a marine scattering sensor was first reported by Sullivan *et al.* [5] and also used in Twardowski *et al.* [6]. They simulated the angular response function by partitioning the entire sampling volume into small elementary volumes, each of which is treated as an independent, well-defined scattering volume for which the VSF is assessed. The sum of the weighting for those elementary volumes that have the same scattering angle gives the angular response function for that angle. While both methods are valid, there are two issues that need to be addressed. The first issue is that neither of the response functions derived from the two methods satisfies Eq. (2), and hence each must be manually normalized for practical applications. The second issue, which is more challenging, is how do we validate a computed  $W_N$  and what are its uncertainties?

This study aims to derive the angular response functions with a focus on addressing these two issues. First, we show mathematically that a properly derived angular response function should automatically satisfy the normalization condition stipulated by Eq. (2). Second, we use a Monte Carlo photon tracing code to corroborate the  $W_N$  simulated for two commercial fixed-angle backscatter devices, namely, HydroScat6 (HOBI Labs) and ECO-BB (Sea-Bird Scientific, Inc.). Third, we test  $W_N$  derived for ECO-BB using the laboratory measurements of scattering by microbeads of NIST-traceable standard sizes. Lastly, we deduce that the normalization factor for deriving  $W_N$  has a physical connotation related to path length attenuation that a scattering sensor must account for in practical applications.

## 2. METHOD AND DATA

### A. Determining the Angular Response Function

We followed the Sullivan *et al.* [5] approach, which partitions the sampling volume into elementary volumes for which the VSF is simulated. A conceptual diagram of this approach is provided in Fig. 1.

If light source emits a radiant flux  $P_S$  (W) within its FOV that forms a solid angle  $\Omega_S$  (sr), the irradiance  $dE$  ( $\text{W m}^{-2}$ ) received by an elementary scattering volume  $dV$  is

$$dE = \frac{P_S t_S d\Omega_S}{\Omega_S dA}, \quad (4)$$

where  $d\Omega_S (= \frac{dA \cos \theta_S}{r_S^2})$  is the solid angle subtended by  $dV$  w.r.t. the source,  $dA (= dx dy)$  is the area illuminated by the light, and  $t_S (= \exp(-cr_S))$  is the radiant transmittance from the source to  $dV$  and  $c$  ( $\text{m}^{-1}$ ) is the beam attenuation coefficient. Following Eq. (1) and denoting the VSF of  $dV$  as  $\beta(\Theta(dV))$ ,

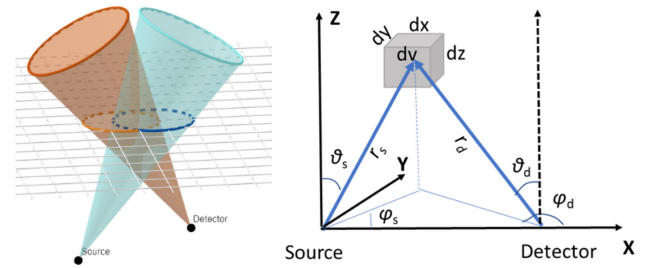


**Fig. 1.** (a) Schematic diagram showing scattering geometry. A horizontal thin slab (gray grids) of thickness  $dz$  forms two ellipses at the intersections with the light source (blue) and detector (red) conic volumes. Moving the slab vertically, accumulation of the intersection of the two ellipses forms the sampling volume. (b) An infinitesimal scattering volume  $dV (= dx dy dz)$  taken from the intersection of the two ellipses is placed in an arbitrarily chosen coordinate system with the light source at the origin and the detector on the  $x$  axis. The line vectors from the source and the detector to  $dV$ ,  $r_S$  and  $r_D$ , have zenith angles of  $\theta_S$  and  $\theta_D$ , and azimuth angles of  $\phi_S$  and  $\phi_D$ , respectively.

where  $\Theta(dV)$  signifies that the actual scattering angle is determined by paths from the source to  $dV$  and from  $dV$  to the detector, the radiant intensity scattered by  $dV$ ,  $dI$  ( $\text{W sr}^{-1}$ ) is

$$dI = dE dV \beta(\Theta(dV)) = \frac{P_S t_S d\Omega_S}{\Omega_S dA} dV \beta(\Theta(dV)). \quad (5)$$

Equations (4) and (5) are for an arbitrary elementary volume  $dV$ . Let us define an elementary volume to represent the mean conditions of all the elementary volumes. This elementary volume has a mean volume of  $dV_{ave}$ , receives a mean irradiance  $dE_{ave}$  from the light source, and scatters a mean radiant intensity of  $dI_{ave}$  received by the detector. These three average quantities can be calculated as

$$dV_{ave} = \frac{\oint_V dV}{N}, \quad (6)$$

$$dE_{ave} = \frac{\oint_V dE dA}{\oint_V dA} = \frac{P_S}{\Omega_S} \frac{\oint_V t_S d\Omega_S}{\oint_V dA}, \quad (7)$$

and

$$dI_{ave} = \frac{\oint_V dI d\Omega_D t_D}{\oint_V d\Omega_D t_D} = \frac{P_S}{\Omega_S} \frac{\oint_V \frac{d\Omega_S d\Omega_D t_S t_D}{dA} dV \beta(\Theta(dV))}{\oint_V d\Omega_D t_D}, \quad (8)$$

where  $N$  represents the total number of elementary volumes,  $d\Omega_D = \frac{dA \cos \theta_D}{r_D^2}$  is the solid angle formed by  $dV$  w.r.t. the detector,  $t_D = \exp(-cr_D)$ , and  $\oint_V$  represents the integration/summation over the entire scattering volume ( $V$ ). From these three average quantities, we define an average VSF  $\beta_{ave}$  as

$$\beta_{ave} = \frac{dI_{ave}}{dE_{ave} dV_{ave}} = \frac{\oint_V dA \oint_V \beta(\Theta(dV)) d\Omega_S d\Omega_D t_S t_D \frac{dV}{dA}}{dV_{ave} \oint_V d\Omega_S t_S \oint_V d\Omega_D t_D}. \quad (9)$$

Equation (9) shows the key relationship of how the scattering by each elementary volume is weighted to produce the average VSF. Defining

$$W(dV) = \frac{d\Omega_S d\Omega_D t_S t_D}{dA}, \quad (10)$$

$$W_T = \frac{dV_{ave} \oint_V d\Omega_S t_S \oint_V d\Omega_D t_D}{\oint_V dA}, \quad (11)$$

and

$$W_{NV}(dV) = \frac{W(dV)}{W_T}, \quad (12)$$

we have

$$\beta_{ave} = \oint_V \beta(\Theta(dV)) W_{NV}(dV) dV. \quad (13)$$

Applying mean value theorem to Eq. (13), we have

$$\beta_{ave} = \beta_{mean} \oint_V W_{NV}(dV) dV. \quad (14)$$

Strictly speaking,  $\beta_{ave}$  and  $\beta_{mean}$  are not the same because they are defined differently. But for a well-defined scattering volume that encompasses a narrow range of scattering angles, their values should be close. Therefore,

$$\oint_V W_{NV}(dV) dV = \frac{\beta_{ave}}{\beta_{mean}} \approx 1. \quad (15)$$

Now we have the response function  $W_{NV}$  defined for each elementary scattering volume.  $W$  has units of  $\text{sr}^2 \text{m}^{-2}$ ,  $W_T \text{sr}^2 \text{m}$ ; therefore,  $W_{NV}$  has units of  $\text{m}^{-3}$ . Also,  $W_{NV}$  derived this way has the inherent property required for a response function, i.e.,  $\oint_V W_{NV}(dV) dV \approx 1$ .

For practical applications,  $W_{NV}(dV)$  for each elementary scattering volume needs to be converted to a response function for each scattering angle. Mathematically, this process can be summarized as, starting from Eq. (13),

$$\begin{aligned} \beta_{ave} &= \int_{\theta_{min}}^{\theta_{max}} \oint_{\Theta(dV) \subseteq \theta \pm d\theta/2} \beta(\Theta(dV)) W_{NV}(dV) dV \\ &= \int_{\theta_{min}}^{\theta_{max}} \beta(\theta) \oint_{\Theta(dV) \subseteq \theta \pm d\theta/2} W_{NV}(dV) dV \\ &= \int_{\theta_{min}}^{\theta_{max}} \beta(\theta) W_N(\theta) d\theta. \end{aligned} \quad (16)$$

Here and throughout this study, we have assumed azimuthal symmetry of the VSF, i.e.,  $\beta(\theta)$  is the same for different azimuth angles because orientation of molecules and particles in natural environments are generally randomly distributed [7]. The first equality in Eq. (16) can be explained as: the total range of scattering angles formed by all  $dV$ 's within the scattering volume represents the angular range of the scattering that the instrument responds to. We denote this angular range as  $[\theta_{min}, \theta_{max}]$  and partition it into a series of infinitesimal intervals. The second and third equality state that for an arbitrary, infinitesimal angular interval from  $\theta - d\theta/2$  to  $\theta + d\theta/2$ , within which  $\beta$  can be assumed constant, find all the  $dV$ 's that produce scattering angles within this range, and compute  $W_N(\theta)$  as

$$W_N(\theta) d\theta = \oint_{\Theta(dV) \subseteq \theta \pm d\theta/2} W_{NV}(dV) dV. \quad (17)$$

$W_N(\theta)$  is the final angular response function and has units of  $\text{rad}^{-1}$  (or  $\text{degree}^{-1}$ ). It also satisfies the normalization condition stipulated in Eq. (2), i.e.,

$$\begin{aligned} \int_{\theta_{min}}^{\theta_{max}} W_N(\theta) d\theta &= \int_{\theta_{min}}^{\theta_{max}} \oint_{\Theta(dV) \subseteq \theta \pm d\theta/2} W_{NV}(dV) dV \\ &= \oint_V W_{NV}(dV) dV \approx 1. \end{aligned} \quad (18)$$

## B. Geometric Configuration of the Sensors

We performed the theoretical derivation of  $W_N$  for two commercial backscatter sensors, HydroScat-6 (HOBI Labs) and ECO-BB (Sea-Bird Scientific, Inc.). The schematic diagrams for two sensors are shown in Fig. 2.

The schematic diagrams shown in Fig. 2 were used for Monte Carlo simulation. They were developed based on the design blueprints provided to us by the manufacturers and consider the path of photons across different media as well as the size and the FOV of both the light source (LED) and detectors. Conceptually, the combined optical effect of all these geometric objects shown in Fig. 2 can be represented by two cones [5], one for the LED and the other for the detector. This simplified

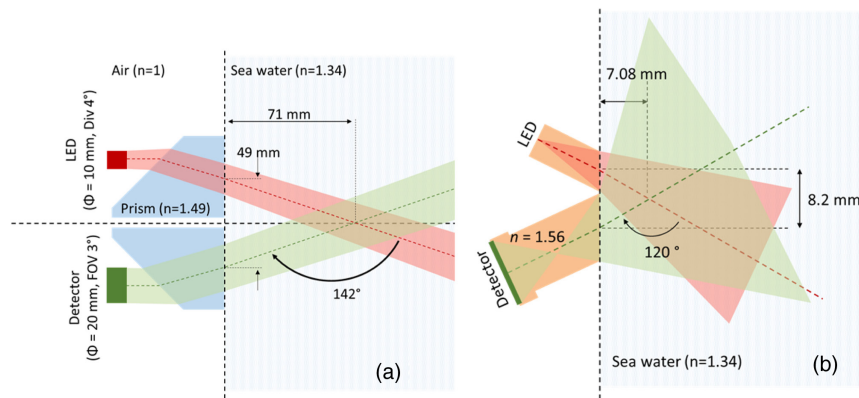


**Fig. 2.** Schematic diagrams for the (a) HydroScat-6 and (b) ECO-BB. Geometric objects include a light source (LED) and detector, different media with their refractive indices ( $n$ ), and light paths (lines). Though not appearing conspicuously, the refraction of light across the sensor–water interfaces is considered and drawn in both diagrams.

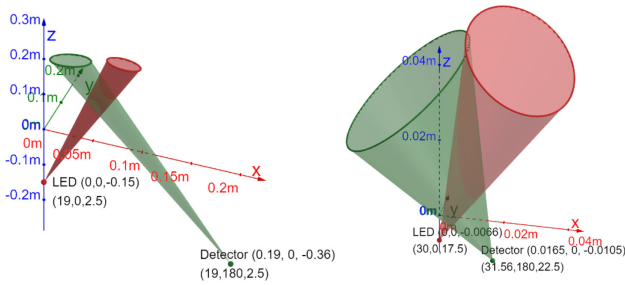


**Fig. 3.** Simplified diagram using cones to represent the FOV of the light source (LED) and the detector of the (left) HydroScat-6 and (right) ECO-BB. The coordinate system is defined with the sensor face on the  $x-y$  plane and the  $z$  direction pointing outward. In the legend, the first triplet is the  $(x, y, z)$  coordinate of the vertex of the cone and the second triplet defines the orientation of the cone (zenith angle of the cone axis, azimuth angle of the cone axis, half-angle of the cone). Notice the difference of the scales between left and right.

diagram for each backscatter sensor is shown in Fig. 3 and was used for determining  $W_N$  of the two sensors.

Note that the locations and size of the mathematical LED and detector cones in the simplified diagram often do not align with their physical, original counterparts. For example, the vertex locations of the LED and detector cones for HydroScat-6 are 19 cm apart in the  $x$  direction and 11 cm apart in the  $z$  direction, which were derived to ensure the conic intersections at the face of the sensor match the actual footprints of the LED and the detector of the sensor. Also, the physical FOV of the detector in ECO-BB has a half-angle of  $42.5^\circ$ . A Monte Carlo ray tracing using the ECO-BB optical setup shown in Fig. 2(b) indicated that its effective FOV has a half-angle =  $22.5^\circ$ , which is used in this study. As illustrated in Fig. 3, two sensors differ significantly in their design and hence how the scattering is measured. The FOVs of both LED and detector in HydroScat-6 have a half-angle of  $2.5^\circ$ , much smaller than those of ECO-BB, which is  $17.5^\circ$  for the source and  $22.5^\circ$  for detector. The intersection of the two cones defined for each sensor in Fig. 3 defines its sampling volume.

**C. Monte Carlo Simulation**

Monte Carlo simulations were performed using the SimulO software [8]. The geometric definition of the sensors shown in Fig. 2 is identical to that used previously [2]. We did not separate water and particles and only considered their cumulative optical effects in scattering and absorption. We simulated the response of each sensor in water for a variety of conditions, with absorption coefficients ( $a$ ) varying from 0 to  $40\text{ m}^{-1}$ , scattering coefficients ( $b$ ) from 0.1 to  $100\text{ m}^{-1}$ , and phase function represented by Fournier–Forand (FF) [9] with backscattering ratios from 0.5% to 5%. The results include the distribution of scattering angles of photons reaching the detector after undergoing single and multiple scattering. Additional simulations were conducted for HydroScat-6, where we reproduced the calibration experiment [4] by moving a Lambertian plaque at various distances from the sensor. The result of this simulation is the proportion of photons detected as a function of the position of the plaque.

**Table 1. Specification of Nanosphere Polystyrene Beads (Thermo Scientific) Used in the Experiment<sup>a</sup>**

Cat. Number	$\mu\text{ND}$ (nm)	$\mu\text{D}$ (nm)	$\delta\text{D}$ (nm)	$\sigma\text{D}$ (nm)
3100A	100	100	3	7.8
3300A	300	300	6	5
3500A	500	510	7	9.2
3700A	700	702	6	4.9
3900A	900	903	12	4.1

<sup>a</sup>The beads with a nominal diameter ( $\mu\text{ND}$ ) are normally distributed, with an actual diameter  $\mu\text{D} \pm \delta\text{D}$  (95% confidence interval) that is NIST-traceable and a standard deviation  $\sigma\text{D}$ .

**Table 2. Spectral Characteristic of the ECO-BB3 S/N 1502 as Measured with a Hyperspectral Radiometer and Fit to a Gaussian Function<sup>a</sup>**

Nominal Wavelength [nm]	Best-Fit Central Wavelength [nm]	$\sigma_\lambda$ [nm]	FWHM [nm]
470	473.0	11.9	28.0
532	541.3	16.0	37.7
650	647.7	10.9	25.7

<sup>a</sup>The standard deviation  $\sigma_\lambda$  and FWHM at each wavelength are also listed.

**D. Laboratory Measurements**

With five nominal size NIST-traceable beads (Table 1), we performed an addition series in a large (60 L) dark container filled with deionized water. Beads were sonicated prior to use. An ECO-BB3 sensor (SN = 1052) was immersed in a container measuring the scattering at three spectral bands with nominal wavelengths of 470, 532, and 650 nm (see Table 2 for the measured wavelengths and their dispersion). A pump was used to pump the mixture of beads and water through the attenuation side and flow sleeve of a WETLabs ac-9 absorption and attenuation meter. The pump was also used to homogenize the samples. Approximately 3–4 additions of each bead were performed, from which we derived the regression between the ECO-BB signal at its specific wavelengths (units of counts) and the beam attenuation at another given wavelength (units of  $\text{m}^{-1}$ ). The slope of this regression represents the measured change of counts per change of beam attenuation ( $\text{counts}/\text{m}^{-1}$ ) as a function of bead size as well as wavelength of each sensor. We used a Mie code (translated to MATLAB from that of Bohren and Huffman [7]) to compute the theoretical response of the sensor given its angular and spectral response and taking into account the finite size distribution of the beads as reported by the manufacturer. The index of refraction of these polystyrene beads is based on Jones *et al.* [10], as they agreed with those of Bateman *et al.* [11], obtained using a different method. The index of refraction of water is based on Quan and Fry [12].

**3. RESULTS**

While the method we developed is not specific to a particular sensor, in this study we focus on presenting results estimated for the two commercial backscatter sensors: HydroScat-6 and ECO-BB.

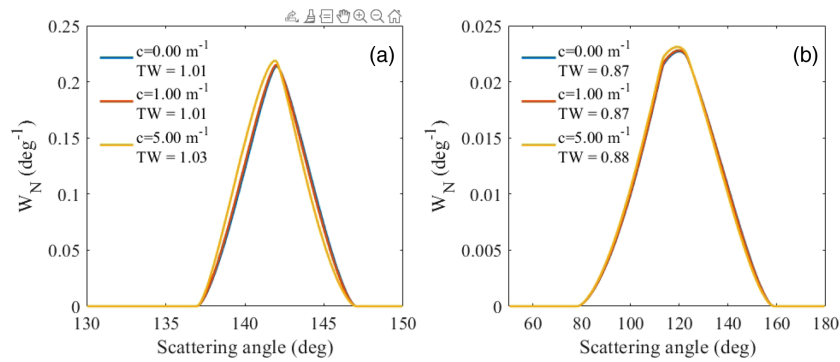


**Fig. 4.** Angular response function  $W_N$  determined mathematically as a function of scattering angle with three different attenuation coefficient ( $c = 0, 1, \text{ and } 5 \text{ m}^{-1}$ ) values for the (a) HydroScat-6 and (b) ECO-BB. TW in the legend is the integrated value of  $W_N$  w.r.t. to scattering angle. Note that the scales of the  $x$  and  $y$  axis are different between the two panels. See [Data File 1](#) and [Data File 2](#) for underlying values for HydroScat-6 and ECO-BB, respectively.

### A. Angular Response Function

The angular response functions,  $W_N(\theta, c)$ , calculated mathematically using Eqs. (12) and (17) for two sensors for waters with three attenuation coefficient values, are shown in Fig. 4. HydroScat-6 [Fig. 4(a)] measures scattering at angles from  $137^\circ$  to  $147^\circ$  with an average scattering angle of  $142^\circ$  and a full width at half-maximum (FWHM) of  $4.6^\circ$ . ECO-BB [Fig. 4(b)] measures the scattering at a much wider range, from  $80^\circ$  to  $160^\circ$ , with an average scattering angle of  $120^\circ$  and an FWHM of  $37^\circ$ . For both sensors,  $W_N$  remains approximately the same for  $c$  values up to  $1 \text{ m}^{-1}$ , but shifts slightly to smaller angles as  $c$  increases further. For example, the average scattering angle is reduced by  $0.5^\circ$  for HydroScat-6 when  $c$  is  $10 \text{ m}^{-1}$  and for ECO-BB when  $c$  is  $5 \text{ m}^{-1}$ . A similar observation was also reported previously [2]. Because the differences among the  $W_N$ 's calculated for various  $c$  values are relatively small comparing to their overall shape, we will use  $W_N$  calculated for  $c = 1 \text{ m}^{-1}$  for both sensors for the rest of the study unless the value of  $c$  is explicitly stated.

The integration of  $W_N$ , i.e.,  $TW = \int_{\theta_{\min}}^{\theta_{\max}} W_N(\theta) d\theta$  is close to unity for HydroScat-6, whereas TW is about 0.87 for ECO-BB. This is probably owing to the difference in the angular range that the two sensors see. Over a smaller angular range, Eq. (15) is a valid assumption, where  $\beta_{\text{ave}}$  defined in Eq. (9) is approximately the same as  $\beta_{\text{mean}}$  defined in Eq. (14). On the other hand,  $\beta_{\text{ave}}$  and  $\beta_{\text{mean}}$  could be different for sensors such as ECO-BB, which probes a wider angular range. As shown in Fig. 4(b), this difference is about 12%. This also means  $W_N$  determined for ECO-BB needs to be renormalized for practical applications.

As defined in Eq. (10), the response function at a distance  $Z$ ,  $W(Z)$ , is proportional to  $\frac{A(Z)}{Z^4}$ , where  $A(Z)$  represents the scattering area at distance  $Z$ . To gain a better understanding of how the angular response function is formed, we include two animation videos ([Visualization 1](#) for HydroScat-6, [Visualization 2](#) for ECO-BB) showing the change of scattering area and the buildup of response function as the distance from the sensor increases. For both sensors, the distance is the primary factor determining the scattering angles, which increase with the distance in general [Fig. 5(a)]. The range of scattering angles at a particular distance depends on the area of intersection (i.e., the scattering area) at this distance [Fig. 1(a)] between

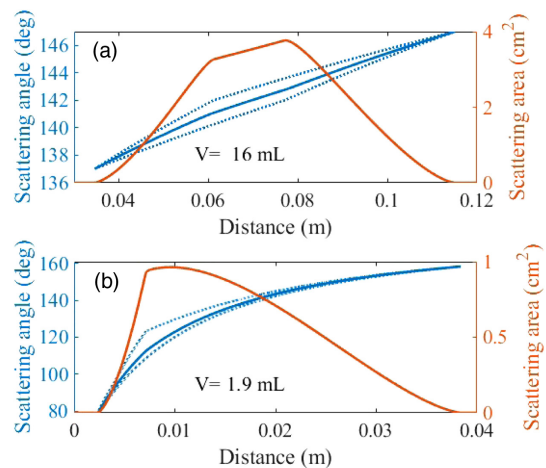


**Fig. 5.** Variations of scattering angle (mean, blue lines; minimal and maximal, blue dotted lines) and scattering area (red curves) derived for the (a) HydroScat-6 and (b) ECO-BB. The total volume of water ( $V$ ) that each sensor probes is calculated by integrating area over distance.

the detector FOV and LED illumination cone. The greater a scattering area is, the greater is its contribution to the response function. For HydroScat-6, a relatively greater scattering area occurs at depths between approximately 6 and 8 cm from the sensor, where the scattering angles vary between  $140^\circ$  and  $144^\circ$ . These two distances correspond to the bending points of the red curve in Fig. 5(a) that have discontinuous slopes. Between these two distances, the LED illumination cone is fully enclosed by the detector FOV; outside of these two distances, the LED illumination cone is only partially enclosed by the detector FOV. For ECO-BB, relatively greater scattering areas are located at distances from 0.7 to 1.5 cm, which have scattering angles ranging from approximately  $100^\circ$  to  $140^\circ$ . The range of depths that each sensor sees also differs significantly. ECO-BB can only see the water no more than 4 cm away, whereas HydroScat-6 probes water at depths from 4–12 cm. From the scattering area, it is straightforward to calculate the total scattering volume. Even though ECO-BB has approximately 8 times wider angular range than HydroScat-6 ( $80^\circ$  versus  $10^\circ$ ), the former probes a much smaller volume than the latter (1.9 mL versus 16 mL).

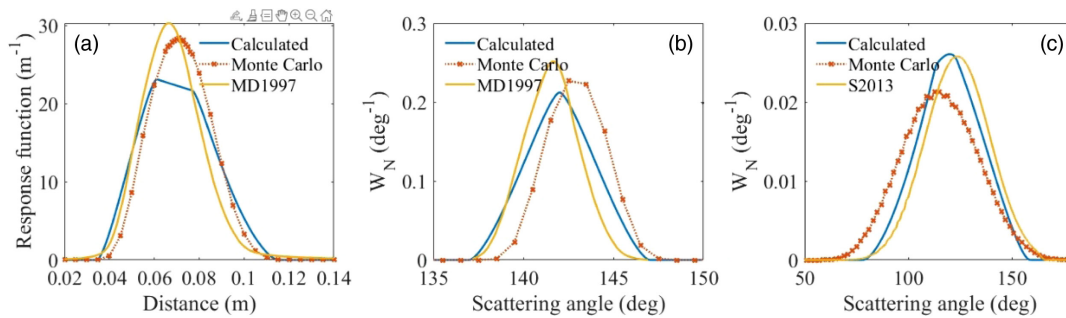


**Fig. 6.** Comparison of the response functions that are calculated and Monte Carlo-simulated in this study with the others. (a) Response functions versus distance calculated, simulated for  $c = 0.01 \text{ m}^{-1}$ , and measured in distilled water by Maffione and Dana [4] (MD1997) for the HydroScat-6; (b) response functions versus angle ( $W_N$ ) for the HydroScat-6; MD1997 was estimated from that in (a) by converting its distance to mean scattering angle using Fig. 5(a). (c) Response functions versus angle ( $W_N$ ) determined in this study and calculated by Sullivan *et al.* [5] (S2013) for the ECO-BB; Monte Carlo results in (b) and (c) represent the average single-scattering values for  $a < 1 \text{ m}^{-1}$ .

## B. Validation

For validation, we compare the calculated response function with the single-scattering Monte Carlo result described in Section 2.C by averaging all the simulations with  $a < 1 \text{ m}^{-1}$ , the response function that Maffione and Dana [4] measured using a Lambertian plaque in distilled water for HydroScat-6, and the response function that Sullivan *et al.* [5] calculated for ECO-BB (Fig. 6). Note that for the effect of attenuation on the angular response function, the combination of single scattering and  $a < 1 \text{ m}^{-1}$  in Monte Carlo simulation is equivalent to our calculation for  $c < 1 \text{ m}^{-1}$ . Averaging the Monte Carlo results simulated for different IOP settings increases the signal-to-noise ratio, particularly for HydroScat-6, for which the narrow FOV has significantly limited the number of photons received by the detector.

For HydroScat-6, we first examine the response function as a function of distance because that was how the measurements were conducted [Fig. 6(a)]. There is general agreement among the calculated, Monte Carlo-simulated, and the measured response functions, all indicating that water at depths from 4 to 12 cm contributes to the scattering, with the peak contribution located between 6 and 8 cm [Fig. 6(a)]. However, the three depth-response functions differ slightly in the mean depth, which are 0.070, 0.072, and 0.069 m for the calculated, Monte Carlo, and measured response functions, respectively. The calculated response function also shows a broader peak, which corresponds to the shoulder seen in the area versus distance plot in Fig. 5(a). This feature, however, is absent in the results of the Monte Carlo simulation and the measurement, probably because the subtle feature of how area varies with the distance, which can be easily captured in the numerical simulation with adequate spatial resolution, may be averaged out in the Monte Carlo simulation or direct measurement. Note that this broader peak only occurs for the response function when plotted as a function of distance and disappears for the response function when plotted as a function of scattering angles [e.g., see Fig. 4(a)].

We calculated angular response function  $W_N$  corresponding to the measured distance-response function [MD1997 in Fig. 6(a)] by converting distance to mean scattering angle using Fig. 5(a). Figure 6(b) compares this converted  $W_N$  with  $W_N$

determined for HydroScat-6 in this study. All the three  $W_N$  (calculated, Monte Carlo, measured) have mean scattering angles within  $142^\circ \pm 0.5^\circ$  and  $\text{FWHM} = 4.6^\circ, 4.3^\circ,$  and  $3.6^\circ$ , respectively. The calculated and Monte Carlo  $W_N$  agree well with each other [the difference appearing in Fig. 6(b) is exaggerated because of the finer scale used in presenting the data]. That the measured  $W_N$  (MD1997) appears narrower is expected because, as shown in Fig. 5, each distance covers a range of scattering angles, which would be underestimated if each distance is only represented by a mean scattering angle. This also illustrates the limitation in measuring the angular response function using a Lambertian target [4].

For ECO-BB,  $W_N$  calculated in this study is very similar in terms of general shape to that calculated by Sullivan *et al.* [5] [Fig. 6(c)], both having  $\text{FWHM} = 37^\circ$ . This is not surprising because the same approach was used in both studies.  $W_N$  simulated with the Monte Carlo approach, while agreeing with the two calculated results in general, appears to be slightly broader, with  $\text{FWHM} = 45^\circ$ . The mean scattering angle estimated from the response function is  $120^\circ$  for this study, very close to the  $119^\circ$  estimated from the Monte Carlo result. In comparison, the mean scattering angle is  $124^\circ$  in [5]. Uncertainty in determining the exact positions and conic shapes of the light source and detector could explain the differences observed in Figs. 6(b) and 6(c).

We measured the scattering by populations of beads of various sizes using an ECO-BB sensor. Because the angular response function is already accounted for in the measurements, the VSF (in relative units before applying a calibration factor) derived from the measurements should tightly correlate with the VSF calculated using Eq. (2). To test if the angular response function we have derived in this study can be used for the ECO-BB sensor, we calculated the VSF from the Mie theory for different bead populations and evaluate if  $W_N$ -weighted VSFs compare better with the measurements than nonweighted VSFs. We renormalize  $W_N$  for ECO-BB such that it satisfies Eq. (2). The comparison is shown in Fig. 7 in terms of ratio of  $\beta(120^\circ, \lambda_1)$  to  $c(\lambda_2)$ . The ratios calculated with applying  $W_N$  correlate better with the measurements [Fig. 7(a)] than those calculated without applying  $W_N$  [Fig. 7(b)], particularly for beads of larger sizes, for which the VSF become increasingly complex. For linear regression with and without applying  $W_N$ , the correlation

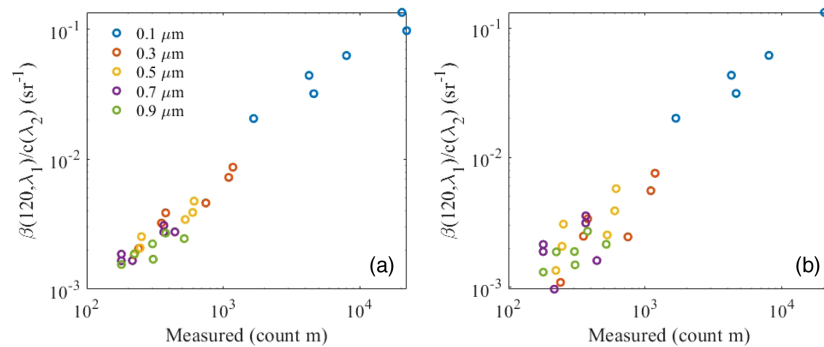


**Fig. 7.** Comparison of ratios of  $\beta(120^\circ, \lambda_1)$  to  $c(\lambda_2)$  that were calculated from Mie theory and measured by the ECO-BB and by an AC-9 sensor for various populations of beads of nominal diameters 0.1, 0.3, 0.5, 0.7, and 0.9  $\mu\text{m}$ . The angular response function was used in deriving  $\beta(120^\circ)$  following Eq. (2) in (a) and not used in (b). For each size, the pairs of wavelengths in nanometers are (470, 440), (470, 650), (532, 440), (532, 650), (650, 470), and (650, 650). The measured values have units of counts in meters (count m).

of determination ( $R^2$ ) decreased from 0.98 to 0.89 and the root mean square error increased from 0.09 to 0.22 (relative units). Results shown in Fig. 7 suggest that  $W_N$  derived for ECO-BB properly captures the angular response of the sensor. In producing the results shown in Fig. 7, we accounted for the spectral dispersion of the ECO-BB sensor (Table 2). This is important because in addition to the size parameter, the refractive indices of the beads and water both vary with the wavelength. Ignoring this spectral variation could lead to an additional difference of up to 10%.

## 4. DISCUSSION

### A. $W_N$ and the Inherent Optical Property

In principle, the VSF is a single-scattering optical property, namely, photons contributing to the VSF should not be scattered either before or after the primary scattering event that the sensor is designed to measure. This is the reason that the beam attenuation coefficient  $c$  is used in computing the radiant transmission  $t_S$  Eq. (4) and  $t_D$  Eq. (8). Under single scattering, the angular response function  $W_N$  is weakly influenced by the attenuation coefficient (Fig. 4), and its dependence on the attenuation coefficient can be safely ignored for  $c < 1 \text{ m}^{-1}$ . We emphasize that both  $W$  [Eq. (10)] and  $W_T$  Eq. (11) vary with  $c$ , as shown in Visualization 1 and Visualization 2. However, their influence cancels in  $W_N (= W/W_T)$ , and hence,  $W_N$  is largely a property of the sensor. This is important because it allows us to use just one response function for most waters in the global ocean.

How  $W_N$  will change in cases with strong absorption that single scattering still applies, but the resultant  $c$  is  $\gg 1 \text{ m}^{-1}$ , for example, in CDOM-dominated waters or in near-infrared spectral region where water molecules absorb strongly? Both our calculation (Fig. 4) and single-scattering Monte Carlo results (not shown) indicate that as  $c$ , or more precisely  $a$ , increases,  $W_N$  tilts to smaller angles. This is because increasing  $a$  shortens the average path length, which, based on the general relationship between distance and scattering angle (Fig. 5), would in turn lower the average scattering angle. Our calculation shows that the reduction of the mean scattering angle is within  $0.5^\circ$  for  $c$  up to  $10 \text{ m}^{-1}$  for HydroScat-6 and up to  $5 \text{ m}^{-1}$  for ECO-BB.

Another question to ask is how  $W_N$  would change when multiple scattering occurs. To answer this question, we compare  $W_N$  estimated by considering between only the single-scattering events and all the scattering events using the Monte Carlo results simulated for HydroScat-6 and ECO-BB. Figure 8 shows the comparison for one of the settings, where the absorption coefficient  $a = 2 \text{ m}^{-1}$ , the backscattering ratio for the FF phase function is 2%, and the total scattering coefficient  $b$  varies from 0.5 to  $20 \text{ m}^{-1}$ , with corresponding single-scattering albedo ( $b/c$ ) varying from 0.2 to 0.9. There is no particular reason for choosing these specific settings other than that their results appear less noisy for HydroScat-6; the same conclusions regarding the effect of multiple scattering (described below) can be drawn for other choices as well.

$W_N$  simulated by considering only single-scattered photons (dotted black lines in Fig. 8) barely change for different  $b$  values, confirming that single-scattering-based  $W_N$  is largely a property of the sensor. Multiple scattering produces a secondary angular response at near-forward directions in addition to the primary response function [colored lines in Figs. 8(a) and 8(c)]. This is expected because the natural VSFs are peaked strongly toward the forward direction [13] and additional scattering beyond the primary scattering would mainly occur at these near-forward directions. The magnitude of the secondary angular response increases with a concomitant decrease of the primary angular response with increasing  $b$  or the fraction of multiple-scattered photons received ( $N_{>1}$ ). Now we take a further examination on how the primary angular response has changed under multiple scattering. To do this, we “ignore” the secondary angular response at the near-forward angles and renormalize the primary angular response functions over the scattering angular range, excluding those near-forward angles. For HydroScat-6 [Fig. 8(b)], renormalized primary  $W_N$  does not change very much for  $b$  up to  $2 \text{ m}^{-1}$  but becomes increasingly broader as  $b > 5 \text{ m}^{-1}$ . For ECO-BB [Fig. 8(d)], renormalized primary  $W_N$  does not change for  $b$  up to  $20 \text{ m}^{-1}$ . In summary, the effect of multiple scattering on  $W_N$  is sensor-specific; it is negligible for HydroScat-6 when  $b < 2\text{--}3 \text{ m}^{-1}$  and negligible for ECO-BB under nearly all conditions that have been simulated. This is because ECO-BB has a much wider FOV and a shorter path length, and hence it receives many more single-scattered photons and relatively fewer multiple-scattered photons than

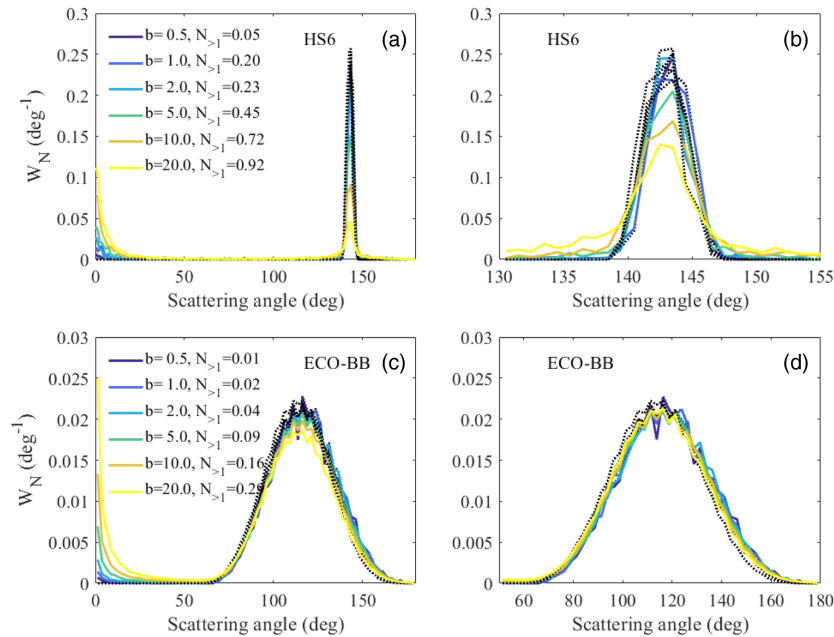


**Fig. 8.**  $W_N$  derived from Monte Carlo simulation for the HydroScat-6 [HS6, (a) and (b)] and ECO-BB [(c) and (d)] with  $a = 2 \text{ m}^{-1}$ , backscattering ratio for FF phase function = 2%, and various  $b$  values. Dotted black lines represent  $W_N$ 's derived by accounting for only those photons that have gone through one scattering event, whereas colored solid lines represent  $W_N$ 's accounting for all the photons received. In (a) and (c),  $W_N$  are normalized over the angular range from  $0^\circ$  to  $180^\circ$  and in (b) and (d)  $W_N$  are normalized over the angular range excluding the near-forward scattering. The legends show the values of  $b$  and the fraction of photons that have gone through multiple scattering before reaching the detector ( $N_{>1}$ ).

HydroScat-6. For example, for the same value of  $b = 20 \text{ m}^{-1}$ , only 29% ( $N_{>1} = 0.29$ ) of received photons by ECO-BB are due to multiple scattering whereas it is 92% for HydroScat-6. As a result, the effect of multiple scattering on  $W_N$  is much more significant for HydroScat-6 than for ECO-BB.

The effect of “ignoring” the near-forward scattering is equivalent to applying the quasi-single-scattering-approximation approach [14] to modify the beam attenuation coefficient  $c$  as

$$c_m = c - 2\pi \int_0^{\theta_F} \beta(\theta) \sin \theta d\theta, \quad (19)$$

where  $\theta_F$  denotes the range of forward scattering to be excluded/ignored in estimating  $c$ .  $\theta_F \approx 12\text{--}13^\circ$  for HydroScat-6 based on the result shown in Fig. 8(b) for  $b = 2 \text{ m}^{-1}$ , below which the effect of multiple scattering on  $W_N$  can be ignored [Fig. 8(b)] and  $\approx 60^\circ$  for ECO-BB based on Fig. 8(c). Note that the value of  $\theta_F$  is greater than the half-angle of the detector's FOV because of multiple scattering. For example, on its way to the detector of HydroScat-6, whose FOV half-angle is  $2.5^\circ$ , a photon can be scattered twice, first at  $2.5^\circ$  and then at  $5^\circ$ , and it still reaches the detector. Because the small-angle scattering occurs frequently in natural environments, its net effect is to increase the angular range of FOV for forward-scattered light.

Another effect of multiple scattering is to tilt  $W_N$  toward larger angles (not shown) by increasing the average path length. The effect of multiple scattering on the general shape of  $W_N$  is opposite that of increasing absorption that shortens the average path length. Therefore, the two effects tend to cancel each other when both conditions are met. However, both result in very subtle changes to the overall shape of  $W_N$  (e.g., see Fig. 4), at

least within the range of inherent optical properties we have considered in this study.

### B. $W_T$ and Calibration of a Scattering Sensor

We have followed the approach presented in Sullivan *et al.* [5], but with an improvement in that we also derived the normalization factor  $W_T$  and demonstrated that  $W_N$  derived in this way automatically satisfies the normalization requirement Eq. (2). While one may argue that the normalization factor  $W_T$  can always be obtained numerically by integrating  $W$ , as done in [5], we show below that  $W_T$  as we have derived it, contains information that is difficult, if not impossible, to glean numerically.

The actual VSF measured by a sensor represents a  $W_N$ -weighted average of the VSF scaled by a factor that needs to be determined through calibration. But what does this calibration factor represent? Continuing from Eq. (5), the total radiant intensity scattered into the FOV of the detector is

$$P_D = \oint_V dI d\Omega_D \tau_D = \frac{P_S}{\Omega_S} \oint_V \frac{\tau_S \tau_D d\Omega_S d\Omega_D}{dA} dV \beta(\Theta(dV)). \quad (20)$$

Rearranging Eq. (20), we have

$$\begin{aligned} \frac{P_D \Omega_S}{P_S} &= \oint_V \frac{\tau_S \tau_D d\Omega_S d\Omega_D}{dA} dV \beta(\Theta(dV)) \\ &= \oint_V \beta(\Theta(dV)) W(dV) dV. \end{aligned} \quad (21)$$

Inserting Eqs. (12) and (13) into Eq. (21) and rearranging, we have

$$\beta_{\text{ave}} = \frac{1}{W_T(c)} \frac{P_D \Omega_S}{P_S} = \frac{1}{W_T(c=0)} \frac{P_D \Omega_S}{P_S} \frac{W_T(c=0)}{W_T(c)}. \quad (22)$$

Denoting

$$S = \frac{1}{W_T(c=0)}, \quad (23)$$

$$\beta_{\text{ave, mea}} = S \frac{P_D \Omega_S}{P_S}, \quad (24)$$

and

$$B(c) = \frac{W_T(c=0)}{W_T(c)}, \quad (25)$$

we have

$$\beta_{\text{ave}} = \beta_{\text{ave, mea}} B(c). \quad (26)$$

The definition of the VSF [Eq. (1)] does not involve the attenuation of light. But for a real scattering sensor, attenuation is always present in both paths from the source to the sample and from the sample to the detector. In Eq. (26),  $\beta_{\text{ave, mea}}$  represents the VSF that is derived directly from the measurements that include the attenuation of light, and hence needs to be applied a correction factor  $B$  to account for loss of photons due to scattering and absorption to estimate the true VSF  $\beta_{\text{ave}}$ .  $B$  is called the sigma correction for the HydroScat sensor.

Now, let us take a further examination of Eq. (24). For a sensor,  $\Omega_S$  has a fixed value. Assuming this sensor also measures the ratio of received energy  $P_D$  to the emitted energy  $P_S$ , the quantity  $\frac{P_D \Omega_S}{P_S}$  gives the mean VSF the sensor was intended to measure after applying the scaling factor  $S$ . While this scaling factor is typically determined through a calibration experiment, as discussed in Section 2.D, for example, it can also be calculated directly, as in Eq. (23). Note that this “ideal” sensor only requires the ratio of  $P_D$  to  $P_S$ , not their respective magnitudes, to be known. More often than not, however,  $P_S$  is not monitored, and  $P_D$  is measured in either voltage or count (assuming a photodetector sensitivity  $Q$ ), then the scaling factor would become  $\frac{S}{P_S Q}$ , which has to be determined through calibration. Also, in this case, the scaling factor could vary through time if either  $P_S$ ,  $Q$ , or both shift.

Unlike the scaling factor, the correction factor  $B$  [Eq. (25)] is purely geometric and does not rely on optical power and sensitivity of the photodetector. We compare the correction factor  $B$ 's calculated for both sensors with the Monte Carlo-simulated correction factors [2] (Fig. 9). To account for multiple scattering, we replaced  $c$  with  $c_m$  in estimating  $B$ . To calculate  $c_m$  with Eq. (19), we used the FF phase function [15], selected based on the backscattering ratio [9] and  $\theta_F = 12.5^\circ$  and  $60^\circ$  for HydroScat-6 and ECO-BB, respectively. The manufacturers typically recommend a correction factor of form  $\sigma = \exp(l \times K)$ , where  $l$  represents a measure of average path length and  $K$  is a measure of attenuation of photons. For HydroScat-6,  $l = 0.1502$  m (from the User's Manual) and  $K = a_{\text{nw}} + 0.4 \times b_{\text{nw}}$  [16], where  $a_{\text{nw}}$  and  $b_{\text{nw}}$  denote non-water absorption and scattering coefficients, respectively. For ECO-BB,  $l = 0.0391$  m and  $K = a_{\text{nw}}$ . Doxaran *et al.* [2] simulated these correction factors using Monte Carlo ray tracing,

recommending  $K = a_{\text{nw}} + 4.34 \times b_{\text{nw}}$  for HydroScat-6 where  $b_{\text{nw}}$  is nonwater backscattering coefficient and  $l = 0.01635$  m for ECO-BB. The manufacturer-provided ( $\sigma$ ) and Doxaran *et al.* [2]-recommended (D2016) correction factors are also compared in Fig. 9. In estimating  $\sigma$  and D2016, we used total values for  $a$  and  $b$  because we did not consider water separately in the simulations.

Even though the two models were derived from entirely different approaches, the correction factors  $B$  agree well with the Monte Carlo results (D2016) for both sensors (Fig. 9). Because D2016 was based on the Monte Carlo result, which was used as the basis of comparison in Fig. 9, it is expected that D2016 will perform well. On the other hand, the correction factor based on this study ( $B$ ) was derived differently, and it performs much better than the manufacturer's model ( $\sigma$ ) for HydroScat-6 [Fig. 9(a)] and ECO-BB [Fig. 9(b)]. Manufacturer-recommended corrections have assumed the path length is fixed and Petzold phase function [13]. Study by Doxaran *et al.* [2] shows that both  $l$  and  $K$  changes with the optical properties of the environment. What is needed for attenuation correction  $\sigma$  is the product of  $l$  and  $K$ , through the value of  $\exp(-l \times K)$ , not the individual values of  $l$  and  $K$ . We have shown that the attenuation correction factor of a scattering sensor is related to the normalization factor of the sensor ( $W_T$ ) and is equivalent to  $B(c_m)$ , representing the ratio of  $W_T(c=0)$  to  $W_T(c_m)$ . In other words, the attenuation correction factor can be computed directly from the geometry of the sensor and the total attenuation coefficient of the environment modified to account for multiple scattering.

From first principles, we derived the angular response function  $W_N$  and its normalization factor  $W_T$ . This theoretical development also prescribes a proper sequence of steps that should be followed in processing the data measured by a backscatter sensor. Step 1, apply the calibration factor to derive  $\beta_{\text{ave, mea}}$  from the raw data. If the ratio of  $P_D$  to  $P_S$  is monitored, the calibration factor is simply  $S$  [Eq. (23)]; otherwise, it needs to be estimated experimentally. Step 2, apply Eq. (26) to estimate  $\beta_{\text{ave}}$  using the attenuation correction factor  $B$  with  $c_m$  Eq. (25). Estimation of  $c_m$  requires knowledge of the VSF at near-forward angles, which can be either measured with a LISST instrument or approximated with an FF function selected using backscattering ratio. Step 3, calculate  $\beta_{\text{p, ave}}(\theta_0) = \beta_{\text{ave}}(\theta_0) - \beta_{\text{w, ave}}(\theta_0)$ , where  $\beta_{\text{p, ave}}(\theta_0) = \int \beta_{\text{p}}(\theta) W_N(\theta) d\theta$  is the average particulate scattering at the nominal scattering  $\theta_0$  that the instrument is designed to measure, and  $\beta_{\text{w, ave}}(\theta_0) = \int \beta_{\text{w}}(\theta) W_N(\theta) d\theta$  is the  $W_N$ -weighted average scattering by pure seawater, which can be predicted with an uncertainty  $<2\%$  as a function of temperature, salinity, and pressure [17–19]. Separation of Steps 2 and 3 is logical and makes physical sense because Step 2 simply reflects the fact that attenuation is caused by both water and particles and hence the attenuation correction needs to be applied to the total scattering signal  $\beta_{\text{ave, mea}}$ . The current attenuation correction schemes recommended for HydroScat-6 and ECO-BB flip Steps 2 and 3, which would result in a correction value  $B' = \frac{B - f_w(\theta_0)}{1 - f_w(\theta_0)}$ , where  $f_w(\theta_0) = \frac{\beta_{\text{w}}(\theta_0)}{\beta_{\text{ave, mea}}}$ . Clearly,  $B'$  becomes more complicated with additional dependence on the fraction

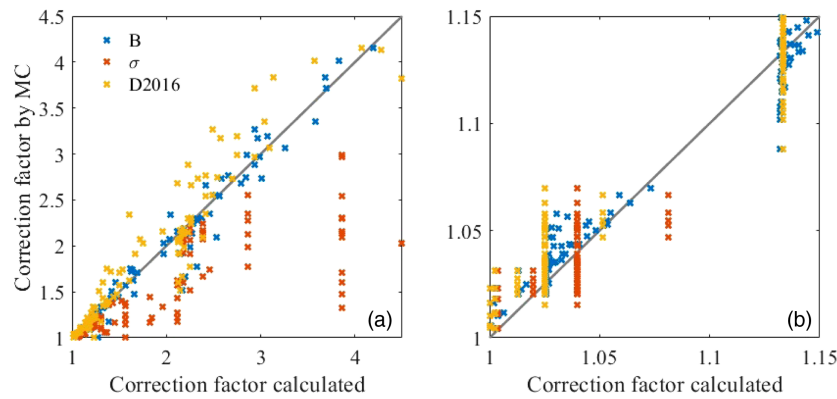


**Fig. 9.** Comparison of the correction factors for two sensors, the (a) HydroScat-6 and (b) ECO-BB. The correction factors derived in this study ( $B$ ), calculated following the models provided by the manufacturers ( $\sigma$ ), and recommended by Doxaran *et al.* [2] (D2016) are evaluated against the Monte Carlo (MC) simulation [2]. The data ranges in both (a) and (b) are for  $c_m < 10 \text{ m}^{-1}$ .

of contribution by water to the total scattering at the nominal angle  $\theta_0$ .

### C. Geometric Setup of a Scattering Sensor

The approach developed in this study depends on characterizing a scattering sensor with simple conic geometries for light source and detector. While always achievable, it was not without challenges, even with the design blueprint of the sensor. For example, we had to deduce the locations of the vertices of the light source and detector for HydroScat-6 from the footprints that they cast on the face of the sensor. Also, for ECO-BB, we estimated the effective FOV of the detector using Monte Carlo simulation. Because of this, there are uncertainties in prescribing the geometric setup for each sensor, which would directly affect our results. For example, the mean scattering angle for ECO-BB is estimated to be  $120^\circ$  in this study, which is in agreement with the geometric centroid angle of the sensor [Fig. 2(b)] and with the Monte Carlo result but differs from the  $124^\circ$  estimated by Sullivan *et al.* [5] [Fig. 6(b)]. On the other hand, once a geometric setup is prescribed for a sensor, it is straightforward to use our method to compute the angular response functions.

The geometry of a scattering sensor changes with the refractive index of the medium it immerses in. Because the refractive index of water varies with the temperature, salinity, and pressure [20], the geometry of the sensor changes with these environmental conditions, for example, when used between fresh, pure water in the lab and seawater in the field. From Snell's law and the empirical equation for the refractive index of seawater [12], we estimated an increase of the refractive index of approximately 0.0063 from fresh water to typical seawater of salinity  $34 \text{ g kg}^{-1}$ , which leads to decreases of the zenith angle and half-angle of the light source and the detector (Fig. 3) by approximately 0.5% for HydroScat-6 and approximately 0.63% and 0.7% for ECO-BB. These changes would in turn increase the mean scattering angle about  $0.18^\circ$  for HydroScat-6 and  $0.36^\circ$  for ECO-BB. As the refractive index of water decreases about 0.0021 for temperature increases from 0 C to 30 C, the effect of temperature on  $W_N$  would be less than that of salinity within their respective natural ranges. Overall, the change of the refractive index of water between typical operation environments has a negligible effect

on  $W_N$ , at least in comparison to the uncertainty in determining the precise geometry of the scattering sensors. However, in waters of extremely high salinity, such as the Dead Sea, where the salinity could reach  $270 \text{ g kg}^{-1}$  [21], the change of refractive index of water could result in an increase of mean scattering angle up to  $1.5^\circ$  for HydroScat-6 and  $2.7^\circ$  for ECO-BB. Another issue associated with dramatic environmental change is the change of transmission at the sensor–water interface. While this is not related to the geometry, it does affect the calibration coefficient needed to be applied for a scattering sensor. Boss *et al.* [21] evaluated and suggested correction for this effect.

We have assumed that the light source is isotropic i.e., Eq. (4). LEDs can have a hot spot such that the intensity emitted is not the same at all angles. This will certainly affect the angular response function. For example, if all the energy is concentrated at one spot, it would effectively reduce the size of illumination cone and hence alter both the shape and magnitude of the angular response function. The intensity distribution of the LEDs used in the backscatter sensors has never been quantified and is likely to cause a difference between sensors, which, however, can be simulated once the distribution is known.

### D. Uncertainty in Deriving Backscattering Coefficients

From the analysis conducted in this study and a recent study on the  $\chi$  factor [22], we estimated an uncertainty budget in estimating the backscattering coefficients from the measurements with the two scattering sensors we have examined (Table 3). The sources of uncertainty are grouped into two categories: calibration and application. For calibration, the uncertainties were estimated using VSF values computed for various bead populations (Table 1) considering (1) the differences in the angular response functions shown in Fig. 6(b) for HydroScat-6 and Fig. 6(c) for ECO-BB; (2) the difference between applying and not applying the spectral response for ECO-BB; and (3) the uncertainty in the mean diameter of the beads. For application, the uncertainties were estimated using the FF phase functions as well as the Monte Carlo simulation [2] based on these FF functions. The application uncertainties consider (1) interpreting measured,  $W_N$ -weighted VSFs using only the value

**Table 3. Uncertainties (in Percent) and Their Sources in Estimating the Angular Backscattering Coefficient Using the HydroScat-6 and ECO-BB Scattering Sensors<sup>a</sup>**

	Calibration				Application				Total (min)	
	Angular	Spectral	Size	$\sigma$ cor.	D2016	B cor.	Angular	$\chi$	VSF	$b_b$
HydroScat-6	2.4	–	6.3	6.1, 25	1.1, 4.2	1.8, 3.7	<0.1	8.0	2.7	8.5
ECO-BB	4.3	2.0	2.0	0.8, 10	1.0, 2.1	0.8, 0.6	8.0	2.2	8.3	8.6

<sup>a</sup>For  $\sigma$ , D2016, and B corrections, the first and second values are for  $c_m$  ( and )  $1 \text{ m}^{-1}$ , respectively. See text for details.

at the centroid scattering angle; (2) applying the attenuation correction factors using the default method ( $\sigma$  correction), the Doxaran *et al.* [2] method (D2016), and the method developed in this study ( $B$  correction) against the Monte Carlo results [2]; and (3) the natural variability of the  $\chi$  factor at the centroid scattering angle, which is used to scale the measured VSF to obtain the backscattering coefficient. When evaluating the uncertainty associated with the attenuation correction factor, we considered two cases: the modified attenuation coefficient Eq. (19)  $c_m < 1 \text{ m}^{-1}$  representing relatively clear waters, and  $c_m > 1 \text{ m}^{-1}$  for more turbid waters.

The distribution of uncertainties varies with the sensor. Because of its relatively long path length, the major uncertainty for HydroScat-6 is due to the attenuation correction. Comparing to the Monte Carlo results [2], the default,  $\sigma$  correction method would induce an average error of 6.1% and 25% in relatively clear and turbid waters, respectively, which can be reduced to 1.8% and 3.7%, respectively, when the  $B$  correction method proposed in this study [also see Fig. 9(a)] is used. In contrast, the uncertainty of  $\sigma$  correction for ECO-BB, whose path length is much less than that of HydroScat-6, is <1% in relatively clear waters but increases to 10% in more turbid waters because of increased optical depth. The  $B$  correction for ECO-BB has an uncertainty <1% in both clear and turbid waters [also see Fig. 9(b)]. Derived from totally different approaches, D2016 and  $B$  corrections have comparable uncertainties in both types of waters for HydroScat-6 and in clear waters for ECO-BB;  $B$  method performs slightly better than D2016 in turbid waters for ECO-BB.

The main uncertainty for ECO-BB arises from the angular response function owing to its wide FOV and manifests in both calibration and application. In calibration, the uncertainty in the exact shape of  $W_N$  among the three shown in Fig. 6(c) could induce an error of 4.3%. We acknowledge that this uncertainty can be reduced or eliminated with a better knowledge of the optical setup of the sensor and hence a more precise estimation of  $W_N$ . In application, the measured VSFs represent  $W_N$ -weighted values, which if interpreted as the VSFs just at the centroid scattering angle would introduce an average error of 8% for ECO-BB. The uncertainty due to angular response function for HydroScat-6 is 2.4% in calibration and negligible in application.

There is uncertainty in the mean diameter of a microbead population used in calibration. This uncertainty will translate to an uncertainty of 2.0% for ECO-BB. HydroScat-6 is typically calibrated using a Lambertian target of an assumed reflectivity at various distances to emulate the change of scattering angles [4]. In this case, the uncertainty in calibration would be mainly due to the difference in the VSFs (2.4%) estimated, with  $W_N$

represented by blue and yellow curves in Fig. 6(b), and the uncertainty of the plaque reflectivity (we do not know).

To the best of our knowledge, we are not aware of publications reporting the use of spectral functions of ECO-BB in its calibration. The average uncertainty associated with this omission is 2% but could reach 10% depending on the size of beads used in the calibration. We do not know the spectral function for HydroScat-6 yet.

With its centroid angle at  $120^\circ$ , ECO-BB benefits from a well-known feature of the  $\chi$  factor, which exhibits minimal variability at scattering angles near  $120^\circ$  [23,24]. From VSF measurements by different investigators in a variety of global waters, Zhang *et al.* [22] estimated that natural variability of the  $\chi$  factor is 2.2% at  $120^\circ$ , and increases to 8.0% at  $140^\circ$ , which applies to HydroScat-6.

For measuring the VSFs, the minimal total uncertainties are 2.7% and 8.3% for HydroScat-6 and ECO-BB, respectively. The greater uncertainty in ECO-BB is mainly due to its wide angular response function, making it difficult to interpret the measured VSFs. For subsequent estimates of backscattering coefficient ( $b_b$ ) from the measured VSFs, the minimal total uncertainties are 8.5% and 8.6% for HydroScat-6 and ECO-BB, respectively. The greater increase in uncertainty for HydroScat-6 is because the  $\chi$  factor at  $142^\circ$  (nominal scattering angle for HydroScat-6) has greater uncertainty than at  $120^\circ$  (nominal scattering angle for ECO-BB). In estimating the minimal uncertainty, we have assumed best-case scenarios in both calibration and application, which include: (1) The total calibration uncertainty is 2.4% for HydroScat-6 (assuming Lambertian target with a precisely known reflectivity is used for calibration) and 2.0% for ECO-BB (assuming both angular and spectral functions are applied and hence the only uncertainty is due to bead sizes). (2) The attenuation correction uncertainty is 1.8% for HydroScat-6 and 0.8% for ECO-BB with the  $B$  correction method used in relatively clear waters. These minimal uncertainties also do not include instrumental uncertainties, such as dark current or electron noise in signal, all of which will increase the uncertainty.

## 5. CONCLUSIONS

We derived the angular response function of a scattering sensor that automatically meets the normalization criterion. We computed the response function for two commercial backscatter sensors, HydroScat-6 and ECO-BB. The computed results were corroborated with Monte Carlo simulation and consistent with a laboratory experiment measuring the scattering by microbeads of five different sizes. The angular response function is a property of the sensor and is only marginally affected by the

attenuation of the medium up to  $c$  values of  $10 \text{ m}^{-1}$ . To the best of our knowledge, this is the first time that the angular response function was computed for HydroScat-6, and our computation for ECO-BB shows that its mean scattering angle is  $120^\circ$  instead of the reported  $124^\circ$ . We found scattering volumes of 16 and 1.9 mL for HydroScat-6 and ECO-BB, respectively. Multiple scattering affects the angular response function, but this effect can be corrected for by adjusting the beam attenuation value to account for scattered light at near-forward angles that are also received by the sensor. We also derived the correction factor for the attenuation of light along the path and showed that our method performs better than the default correction methods provided by the manufacturers for the two sensors. The major uncertainty for ECO-BB is associated with its angular response function because of its wide FOV, whereas for HydrScat-6, the main uncertainty is due to attenuation correction because of its relatively long path length.

**Funding.** National Science Foundation (1917337); National Aeronautics and Space Administration (80NSSC19K0723, 80NSSC20K0350, 80NSSC20M0210).

**Acknowledgment.** We thank David Dana for the HydroScat-6 data and James Sullivan for the ECO-BB data that we used for comparison in this work. We thank Ron Zaneveld and Mike Twardowski for their discussion on angular response function. The MATLAB code for computing conic intersection with a plane is based on Ref. [25]. We thank two anonymous reviewers for their comments. XZ thanks NASA and NSF for funding.

**Disclosures.** The authors declare no conflicts of interest.

**Data Availability.** Data underlying the results presented in this paper are available in [Data File 1](#), [Data File 2](#), and Ref. [26] or by contacting XZ.

## REFERENCES

- R. W. Preisendorfer, *Hydrologic Optics: Introduction* (Pacific Marine Environmental Laboratory/NOAA, 1976), Vol. 1, p. 218.
- D. Doxaran, E. Leymarie, B. Nechad, A. Dogliotti, K. Ruddick, P. Gernez, and E. Knaeps, "Improved correction methods for field measurements of particulate light backscattering in turbid waters," *Opt. Express* **24**, 3615–3637 (2016).
- E. Boss, D. Stramski, T. Bergmann, W. S. Pegau, and M. Lewis, "Why should we measure optical backscattering?" *Oceanography* **17**, 44–49 (2004).
- R. A. Maffione and D. R. Dana, "Instruments and methods for measuring the backward-scattering coefficient of ocean waters," *Appl. Opt.* **36**, 6057–6067 (1997).
- J. Sullivan, M. Twardowski, J. R. V. Zaneveld, and C. Moore, "Measuring optical backscattering in water," in *Light Scattering Reviews 7*, A. Kokhanovsky, ed. (Springer, 2013), pp. 189–224.
- M. Twardowski, X. Zhang, S. Vagle, J. Sullivan, S. Freeman, H. Czerski, Y. You, L. Bi, and G. Kattawar, "The optical volume scattering function in a surf zone inverted to derive sediment and bubble particle subpopulations," *J. Geophys. Res.* **117**, C00H17 (2012).
- C. F. Bohren and D. R. Huffman, *Absorption and Scattering of Light by Small Particles* (Wiley, 1983), p. 530.
- E. Leymarie, D. Doxaran, and M. Babin, "Uncertainties associated to measurements of inherent optical properties in natural waters," *Appl. Opt.* **49**, 5415–5436 (2010).
- C. D. Mobley, L. K. Sundman, and E. Boss, "Phase function effects on oceanic light fields," *Appl. Opt.* **41**, 1035–1050 (2002).
- S. H. Jones, M. D. King, and A. D. Ward, "Determining the unique refractive index properties of solid polystyrene aerosol using broadband Mie scattering from optically trapped beads," *Phys. Chem. Chem. Phys.* **15**, 20735–20741 (2013).
- J. B. Bateman, E. J. Weneck, and D. C. Eshler, "Determination of particle size and concentration from spectrophotometric transmission," *J. Colloid Sci.* **14**, 308–329 (1959).
- X. Quan and E. S. Fry, "Empirical equation for the index of refraction of seawater," *Appl. Opt.* **34**, 3477–3480 (1995).
- T. J. Petzold, "Volume scattering function for selected ocean waters," SIO Ref. 72–78 (Scripps Institution of Oceanography, 1972).
- H. R. Gordon, "Simple calculation of the diffuse reflectance of the ocean," *Appl. Opt.* **12**, 2803–2804 (1973).
- G. R. Fournier and J. L. Forand, "Analytical phase function for ocean water," *Proc. SPIE* **2258**, 194–201 (1994).
- Hobi Instrument Services, "HydroSoft 2.95 software for HOBI labs optical oceanographic instruments, user's manual, revision I," (2015).
- X. Zhang and L. Hu, "Estimating scattering of pure water from density fluctuation of the refractive index," *Opt. Express* **17**, 1671–1678 (2009).
- X. Zhang, L. Hu, and M.-X. He, "Scattering by pure seawater: effect of salinity," *Opt. Express* **17**, 5698–5710 (2009).
- L. Hu, X. Zhang, and M. J. Perry, "Light scattering by pure seawater: effect of pressure," *Deep-Sea Res.* **146**, 103–109 (2019).
- R. W. Austin and G. Halikas, "The index of refraction of seawater," SIO Ref. No. 76–1 (Scripps Institute of Oceanography, 1974).
- E. Boss, H. Gildor, W. Slade, L. Sokoletsky, A. Oren, and J. Loftin, "Optical properties of the Dead Sea," *J. Geophys. Res.* **118**, 1821–1829 (2013).
- X. Zhang, L. Hu, D. Gray, and Y. Xiong, "Shape of particle backscattering in the North Pacific Ocean: the  $\chi$  factor," *Appl. Opt.* **60**, 1260–1266 (2021).
- T. Oishi, "Significant relationship between the backward scattering coefficient of sea water and the scatterance at  $120^\circ$ ," *Appl. Opt.* **29**, 4658–4665 (1990).
- X. Zhang, E. Boss, and D. J. Gray, "Significance of scattering by oceanic particles at angles around 120 degree," *Opt. Express* **22**, 31329–31336 (2014).
- S. Calinon and A. Billard, "Teaching a humanoid robot to recognize and reproduce social cues," in *ROMAN 2006—The 15th IEEE International Symposium on Robot and Human Interactive Communication* (2006), pp. 346–351.
- X. Zhang, "MATLAB code for calculating angular response function," Xiaodong Zhang marine optics lab/programs, 2021, <https://sites.google.com/view/xiaodongzhang-marineopticslab/programs>.